Nanoscale

New Topological States in HgTe Quantum Wells from Defect Patterning

Journal:	*Nanoscale*
Manuscript ID	NR-COM-06-2018-004878.R1
Article Type:	Communication
Date Submitted by the Author:	25-Jul-2018
Complete List of Authors:	Fu, Huahua; Huazhong University of Science and Technology, School of Physics Wu, Ruqian; UC Irvine ,

Nanoscale

COMMUNICATION

View Article Online
View Journal | View Issue

Cite this: DOI: 10.1039/xxxxxxxxxx

New Topological States in HgTe Quantum Wells from Defect Patterning†

Hua-Hua Fu,*[a,b] and Ruqian Wu*[a]

Received Date
Accepted Date

DOI: 10.1039/xxxxxxxxxx

www.rsc.org/journalname

To explore new opportunities for the realization of the quantum spin Hall (QSH) effect in two-dimensional (2D) materials, we have constructed a honeycomb geometry (HG) by etching rows of hexagonal holes in HgTe quantum wells (QWs). Theoretical calculations show that multiple Dirac cones can be produced by HG, regardless of whether the band inversion occurs or not. Furthermore, the topological states originating from a narrow HG region in a wide ribbon show strong localization at the physical edges of the ribbon, making them easy for manipulation and exploitation. When the band inversion condition for QW states is satisfied, the topological states generated from two different mechanisms may coexist. Our studies pave a way to produce and control multiple QSH states in 2D materials as desired for the design of innovative spintronic materials.

Quantum spin Hall (QSH) insulators, also known as two-dimensional (2D) topological insulators (TIs), manifest a new state of quantum matter characterized by the presence of conducting helical edge states (HESs) in the bulk band gap.[1–3] The QSH state was first predicted for graphene, but the small spin-orbit coupling (SOC) of carbon atoms makes this important phenomenon undetectable in experiments.[3] A major step toward the realization of the QSH state was achieved by using materials with ąřinvertedąś energy bands, i.e., the bands with two distinct wave function features cross each near the Fermi level. Accordingly, a quantum phase transition was predicted by Zhang *et al*. for HgTe/CdTe quantum wells (QWs), which change to the QSH phase as the thickness of the HgTe layer becomes larger than a critical value (d_c = 7.5 nm).[4–6] It is recognized nowadays that there are two different physical mechanisms for the production of the QSH state, even though both need strong SOC. One is based on the peculiar electronic features of a honeycomb lattice such as graphene, and the other stems from the inverted band structures. For the convenience of discussions below, we call the materials in these two categories type-I and type-II TIs respectively. To search for type-I TIs, ultracold atom honeycomb supperlattices,[7] graphene-like organmetallic lattices,[8] molecular graphene,[9] 2D electron gases covered by a geometric array of gates[10,11] and 2D single-crystalline sheets of semiconductors with honeycomb lattice,[12–14] have been proposed. On the contrary, only very few type-II TIs such as InAs/GaSb heterostructures have been investigated.[15] Nevertheless, experimental observations of the QSH state have only been reported for HgTe/CdTe[6] and InAs/CaSb QWs,[5,16] whereas numerous predictions for type-I TIs remain to be confirmed.

Applications of the QSH state in realistic devices require materials with large topological gaps and high tunability. To this end, it is necessary to employ or combine different physical mechanisms for the design of new topological materials. In this letter, we construct HgTe QWs with defect arrays in a honeycomb lattice. Through tight-binding calculations, we find several unusual topological phenomena which have not reported so far, due to the coherent interplay of the type-I and type-II mechanisms. The band structure shows multiple Dirac cones and nontrivial flat bands, regardless of the status of band inversion, and the Dirac cones from different physical mechanisms can coexist in the same material. The required conditions to realize the coexistence of the two types of Dirac cones are discussed in detail. Furthermore, the topological states produced by defect arrays may extend far away through the non-defected region of the QW to the edges of nanoribbon, which provides a possibility to operate QSH state from far-away terminals. Our findings open doors to realize the coexistence of multiple QSH states with different physical mechanisms and to generate the QSH state with desired properties for device applications.

Following the previous design of HgTe QWs by Bernevig *et al*.,[5]

[a] *Department of Physics and Astronomy, University of California, Irvine, California 92697-4575, United States; E-mail: wur@uci.edu*
[b] *School of Physics, Huazhong University of Science and Technology, Wuhan 430074, Peopleąŕs Republic of China; E-mail: hhfu@hust.edu.cn*

† Electronic Supplementary Information (ESI) available: The band structure of the HgTe-QW ribbon with a row of hexagonal holes, the band structures of Model 3 with the further increasing of HgTe QW thickness, and the transition from the flat bands to the Dirac bands in one HgTe-QW ribbon. See DOI: 10.1039/b000000x/

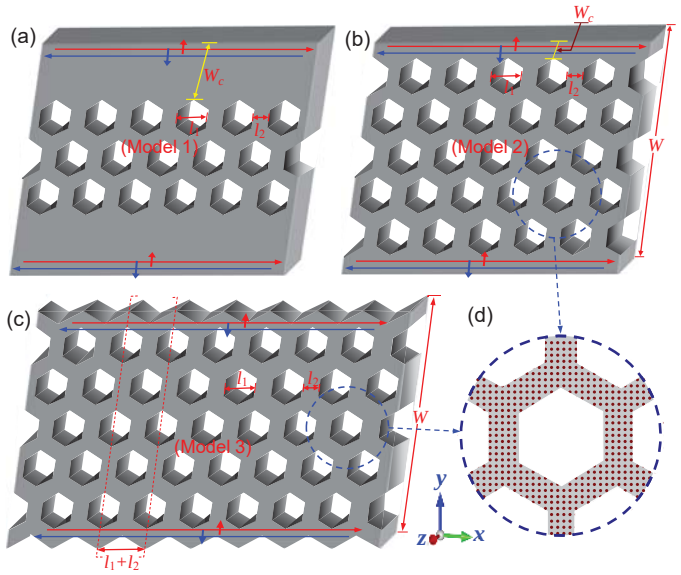

Fig. 1 (a) Model 1: A HgTe QW ribbon with two flat boundaries and three rows of hexagonal holes symmetrically along the ribbon direction. (b) Model 2: A HgTe QW ribbon with five rows of hexagonal holes and two flat boundaries, the structure parameters are set as the same as these in Model 1. (c) Model 3: A HgTe QW ribbon with five rows of holes and two zigzag boundaries to feature graphene-like supperlattices. In the all ribbons, d denotes the QW thickness, l_1 (= 35 nm) denotes the hole width, l_2 (= 25 nm) denotes the distance between two boundaries of the nearest holes, and W refers to the ribbon width. In Model 1 and 2, W_c denotes the distance between the first (last) row of holes and the upside (downside) ribbon boundary. (d) A magnifying diagram of a HgTe hexagonal hole, in which every red dot shows the lattice site mapped by the tight-binding model, the distance between two nearest lattice site is denoted by a (= 5 nm).

we construct two defected HgTe QW ribbons by etching multiple rows of hexagonal holes along the ribbon direction. To see the effect of these superstructures, we first construct Model 1 and 2 with two flat edges, and three and five rows of holes are adopted to form honeycomb lattices, respectively, as shown in Figs. 1a and b. In both models, we denote the hole width with l_1 (= 35 nm) and the distance between two nearest holes with l_2 (= 25 nm), the ribbon width with W, and the distance between the upside ribbon boundary and the nearest row of holes with W_c. To simulate the graphene-like geometry, we further construct Model 3 with two zigzag boundaries based on Model 2. We want to point out the fundamental difference between our models and the HgTe, PbSe or CdSe QWs and superlattices used in some previous studies.[17,18]

The Bernevig-Hughes-Zhang (BHZ) model has been used for studies of HgTe QWs in quantum dots, quantum point contacts and multiple H-shape terminals,[19–21] it is should be also applicable to describe the HgTe layers in our structures, if the contributions of low-energy electrons are mainly considered.[5,22] Based on the symmetry consideration, the effective BHZ Hamiltonian can be mapped into a tight-binding model on a square lattice with four special orbit states $|s,\uparrow\rangle$, $|p_x+ip_y,\uparrow\rangle$, $|s,\downarrow\rangle$ and $|-(p_x-ip_y),\downarrow\rangle$ as follows[23,24]

$$H=\sum_{\mathbf{i}}\varphi_{\mathbf{i}}^{\dagger}E_{\mathbf{i}}\varphi_{\mathbf{i}}+\sum_{\mathbf{i}}(\varphi_{\mathbf{i}}^{\dagger}v_{\mathbf{i}+\delta x}\varphi_{\mathbf{i}+\delta x}+\varphi_{\mathbf{i}}^{\dagger}v_{\mathbf{i}+\delta y}\varphi_{\mathbf{i}+\delta y}+\mathrm{H.c.}), \quad (1)$$

where $\mathbf{i}=(ix,iy)$ is the site index, and δx and δy are unit vectors along the length and width direction, $\varphi_{\mathbf{i}}=(a_{\mathbf{i}},c_{\mathbf{i}},b_{\mathbf{i}},d_{\mathbf{i}})'$ represents the four annihilation operators of electron on the site $\mathbf{i}$ with the above four states, $E_{\mathbf{i}}=\left(\begin{smallmatrix}1&0\\0&1\end{smallmatrix}\right)\otimes\left(\begin{smallmatrix}E_s&0\\0&E_p\end{smallmatrix}\right)$ denotes the on-site potential matrix, $v_{\mathbf{i}+\delta x}=\left(\begin{smallmatrix}1&0\\0&0\end{smallmatrix}\right)\otimes\left(\begin{smallmatrix}V_{ss}&V_{sp}\\-V_{sp}^{*}&V_{pp}\end{smallmatrix}\right)+\left(\begin{smallmatrix}0&1\\0&0\end{smallmatrix}\right)\otimes\left(\begin{smallmatrix}V_{ss}&V_{sp}^{*}\\-V_{sp}&V_{pp}\end{smallmatrix}\right)$, and $v_{\mathbf{i}+\delta y}=\left(\begin{smallmatrix}1&0\\0&0\end{smallmatrix}\right)\otimes\left(\begin{smallmatrix}V_{ss}&iV_{sp}\\iV_{sp}^{*}&V_{pp}\end{smallmatrix}\right)+\left(\begin{smallmatrix}0&1\\0&0\end{smallmatrix}\right)\otimes\left(\begin{smallmatrix}V_{ss}&-iV_{sp}^{*}\\-iV_{sp}&V_{pp}\end{smallmatrix}\right)$. Here, $E_s=C+M-4(B+D)/a^2$, $E_p=C-M-4(B+D)/a^2$, $V_{pp}=(B+D)/a^2$ and $V_{sp}=-iA/2a$, with a (= 5 nm) denoting the lattice constant (see Fig. 1). The SOC is naturally invoked in this Hamiltonian through the spin-orbit coupled p orbitals: $|p_x+ip_y,\uparrow\rangle$ and $|-(p_x-ip_y),\downarrow\rangle$. The parameters A, B, C, D and M depend on the pure QW geometry, and they can be estimated by comparing results of the well-established 8×8 Kane Hamiltonian.[25,26] In the following, we use values A = 364.5 meV nm, B = -686 meV nm^2, C = 0 and D = -512 meV nm^2. The Dirac rest mass M in QWs can be tuned continuously from a positive value $M>0$ for thin QWs with thickness $d<d_c$ to a negative value $M<0$ for thick QWs with $d>d_c$, which corresponds to the topological trivial and nontrivial regions, respectively. To mimic the defected HgTe ribbons with multiple holes and zigzag edges, we remove orbitals of vacant sites from the tight-binding model calculations. The spin-dependent wave-function distributions of the lattice (m, n) can be calculated by $\pm|\Phi_{m,n}|^2=\pm\sum_{k=s,p}\langle\varphi_{m,k,\sigma}|\varphi_{n,k,\sigma}\rangle$, where σ is the spin index, m (n) is the lattice position along the ribbon length (width) direction and the positive (negative) sign refers to the spin-up (-down) state.

To reveal the topological properties, the width size W of Model 1 is set as a general value, i.e., 285 nm (=57a) (see Fig. 1a), and its band structure is calculated for various values of M, ranging from 10 to -20 meV. Some particular properties can be identified from the bands plotted in Fig. 2a to 2c. First, a band gap appears around the Fermi level ($E_F=0$) and the gap decreases with increasing QW thickness, which ascribes the gradual phase transition to TI as the quantum confinement effect decreases in the QWs.[13] Second, the bands show Dirac cones regardless of the value of M, even in the region where HgTe QW has a trivial insulating feature. Since the appearance of the Dirac states here is independent of the thickness of the QW, these states should be produced by the honeycomb lattice of defects, rather than by the band inversion in the QW.[27,28] To support this conclusion, we also study a HgTe QW ribbon with only one row of hexagonal holes, and find that the band inversions when $d>d_c$ is still the prerequisite of the presence of Dirac states, as shown in Fig. S1 in the Supporting Information (SI). Moreover, to grasp the physical nature of these Dirac states, we examine two chosen states, i.e., α_1 and α_2 in the Dirac bands, and plot their spin-dependent wave-function spatial distributions as a function of the lattice position n along the ribbon width in Fig. 2i. It is interesting that these Dirac states are localized at the edges of the QW ribbon, rather than at the edges of the defect sub-ribbon. This suggests an inspiring characteristic of QSH state: the topological states

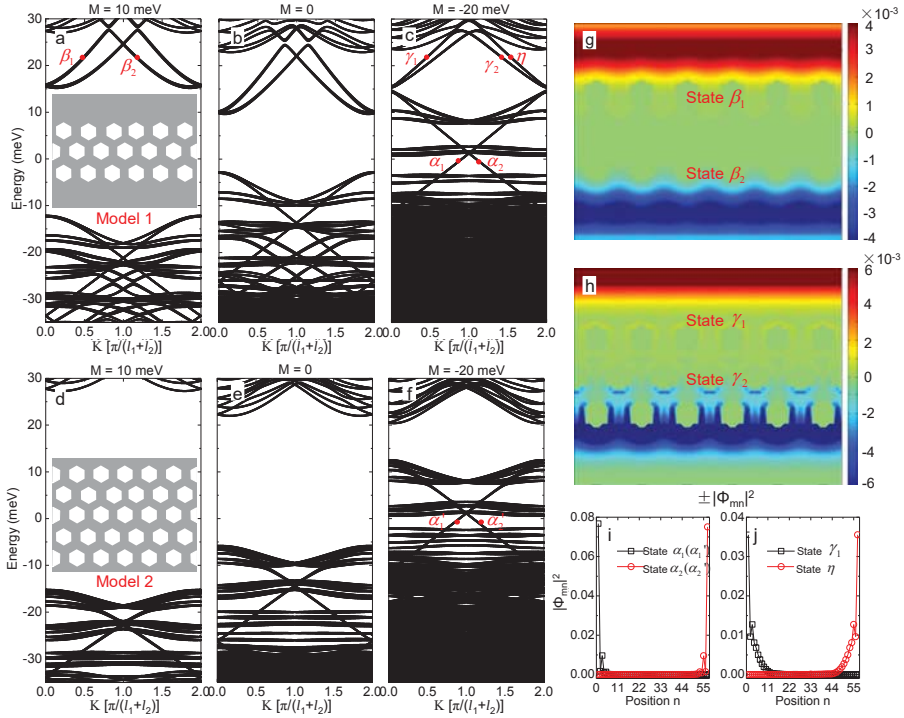

Fig. 2 (a-c) The band structures of Model 1 with two flat boundaries, where W_c = 75 nm. (d-f) The band structures of Model 2 with two flat boundaries and W_c = 25 nm. In these two models, the parameter M is set as 10, 0, and -20 meV to show the increased QW thickness. (g) and (h) The spin-dependent wave-function spatial distributions $\pm|\Phi_{mn}|^2$ of the chosen states β_1 and β_2 (see figure a) and the states γ_1 and γ_2 (see figure c), where ąř+ (-)ąś denotes the distributions of the spin-up (-down) state. (i) and (j) The wave-function distributions of the related edge states α_1 (α_1') and α_2 (α_2') in Model 1 (2) versus the lattice position n along the width direction.

produced by the defect arrays drift to the physical edges of the ribbon, but do not localize at the boundaries of the defect sub-ribbon. The drifting of the above QSH state is tightly related to the particular geometric structure of the model. In fact, Model 1 can be regarded as a graphene-shape supper lattice structure having two wide flat edges, and the QSH state originated from the HG should be localized at the outmost edges of the model[3].

To see the robustness and generality of this drift, we construct Model 2 as illustrated in Fig. 2b, in which two rows of holes are added in the QW ribbon. Interestingly, the Dirac bands remain in the band structures regardless of QW thickness as shown in Fig. 2d to 2f, which confirms further that the Dirac states originate from the honeycomb lattice of defects. Similarly, we choose two Dirac states, i.e., α_1' and α_2' as shown in Fig. 2f, to examine their wave-function spatial distributions. One can see that they have the same localization at the physical boundaries of QW ribbon as α_1 and α_2 of Model 1 (see Fig. 2i). This confirms the robustness of the Dirac states induced by the honeycomb lattice of defects, because the spatial distributions of Dirac states are rather independent of the rows of holes. Since the defect-driven topological states may drift far away from the region where they are created, one may control the transport properties of nanoribbons more easily. For example, we may generate topological states in the conventional insulators with strong SOC, but operate them from distant terminals. Additionally, the band structures of Model 2 show that the additional two rows of holes bring about more flat bands, indicating that the flat bands refer to the circulating edge states around the holes.

Another interesting finding here is that the Dirac cones originating from two different mechanisms can coexist in one system. In Model 1, as the QW thickness increases, eight lowest conduction bands gradually show linear dispersions, as plotted in Fig. 2a to 2c. To perceive the evolution of the topological feature of these states, we analyze their spatial distributions for different M values. Note that the regimes above and below the three rows of holes in Model 1 can be viewed as two pure HgTe QW subribbons with a width of W_c (= 75 nm), as illustrated in Fig. 1a. When M = 10 meV, the spin-up state β_1 and the spin-down one β_2 chosen in Fig. 2a, distribute rather uniformly in the pure HgTe sub-ribbons as drawn in Fig. 2g. This indicates that these two states display as a trivial feature of the conduction states of a semiconductor. As the thickness of the HgTe QW increases to the regime of topological phase transition (M = -20 meV), these conduction bands become more linear. The spin-up state γ_1 and the spin-down one γ_2 tend to behave as edge states that localize at the physical boundaries of the HgTe QW subribbons as shown in Fig. 2h. Apart from these, some supplementary calculations show that as the HgTe QW become thicker, several conduction bands are more linear, as shown in Fig. S2 in the SI. Thus it can be drawn that these newly-developed Dirac bands in Model 1 are generated by the band inversion. Considering the Dirac bands originating from the honeycomb lattice of defects in the low-energy region, Model 1 can be regarded as the first example in which the Dirac cones from two different mechanisms can coexist in the same system.

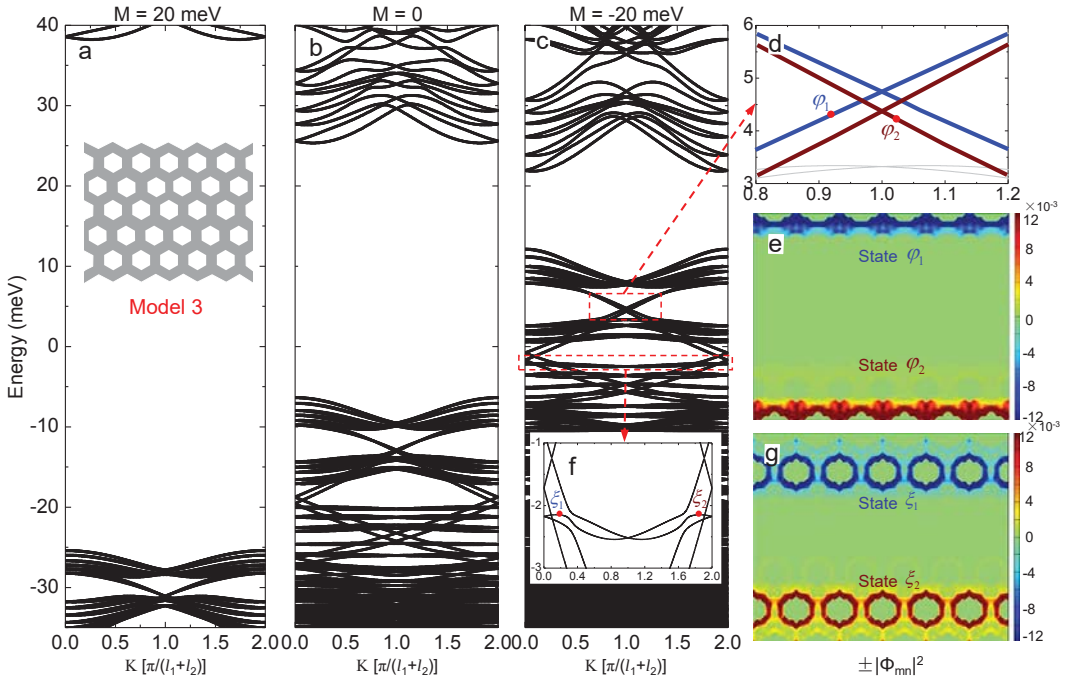

Fig. 3 (a-c) The band structures of Model 3 with two zigzag boundaries and different QW thickness. (d) and (f) The Dirac bands and the flat bands, and some typical states are chosen and labeled as φ_1, φ_2, ξ_1 and ξ_2. (e) The spin-dependent wave-function distributions $\pm|\Phi_{mn}|^2$ of the states φ_1 and φ_2 in the Dirac bands, where ąř+ (-)ąś denotes the distributions of the spin-up (-down) state. (g) The wave-function spatial distributions of the states ξ_1 and ξ_2 in the flat bands, where six repeating units along the ribbon direction are adopted.

The coexistence of two types of edge states opens a door to generate multiple channels of spin transport towards special device applications.

It should be stressed that the finite-size effect occurring in the HgTe QW subribbons is an important factor to influence the coexistence of two types of the Dirac cones. To illustrate this point, we plot the wave-function spatial distributions of two Dirac states (cf. the states γ_1 and η in Model 1) in Fig. 2j. Although these two states retain the typical characteristics of edge states, they extend in a larger region, attributing to the finite-size effect.[29–31] In Model 2, the widths of the HgTe QW sub-ribbons are narrow (i.e., W_c = 25 nm), which makes the bulk states in the Dirac bands of Model 1 disappearing in Fig. 2d to 2f. As a result, it is impossible to reach the coexistence of Dirac states with different mechanisms in Model 2.

Next, to show the robust characteristics of the Dirac states produced by hexagonal defect arrays, the flat boundaries of Model 2 are replaced by two zigzag-like boundaries, which further extends the model to a nearly perfect graphene-shape superlattices (cf. Model 3 in Fig. 1c). Interestingly, the band structures of this example shown in Fig. 3a to c retain all the main features of Model 2 drawn in Fig. 2, including the band gaps and the Dirac cones. Nevertheless, the bands of Model 3 has larger spin-splittings than those of previous models, due to the fact that the zigzag boundaries break the inversion symmetry.[2] Meanwhile, due to the additional electron scatterings along the two zigzag boundaries, the velocity of Dirac electrons in Model 3 decreases. To appreciate the physical nature of the spin-splittings of Dirac bands, we give their spin-dependent wave-function distributions in Fig. 3e for the case with M = -20 meV. Two Dirac states, i.e, the spin-down state φ_1 and the spin-up one φ_2 chosen in Fig. 3d, localize at two physical boundaries, and display as a zigzag-like shape, following the boundary geometry. Moreover, these two spin states have different propagation direction and spin orientation at the opposite boundaries, as shown in Fig. 3e. The spin-momentum lock feature of these edge states confirms further their topologically nontrivial nature. It is well known that the HESs in zigzag graphene ribbons are contributed from atoms near to the edges.[32] However, the HESs shift to the outermost sub-ribbons, making the graphene-like superlattices more attractive for device applications. Additionally, to explore the topological properties of many nearly flat bands of the model, two typical spin states (cf. the states ξ_1 and ξ_2 in Fig. 3f) are chosen to show their spin-dependent wave-function distributions, as plotted in Fig. 3g. We find that these states are localized at the edges of the holes and can convert to the Dirac ones as they are coupled with each other, as shown in Fig. S3 in the SI, supporting the topological characteristic of the flat bands.

Finally, we want to comment on the experimental feasibility for the fabrication and characterization of our model systems. The QSH state of HgTe QWs have already been realized in experiments. Some modifications in the original procedure such as growing HgTe layer on a substrate with rows of hexagonal pillars,[5,6] etching rows of hexagonal holes in the HgTe layer, encouraging some work has already been done for the GaAs QWs.[33] It should be pointed out an artificial graphene in small-period nanopatterned GaAs QWs has already been constructed in a very recent experiment, and the Dirac states from the honeycomb su-

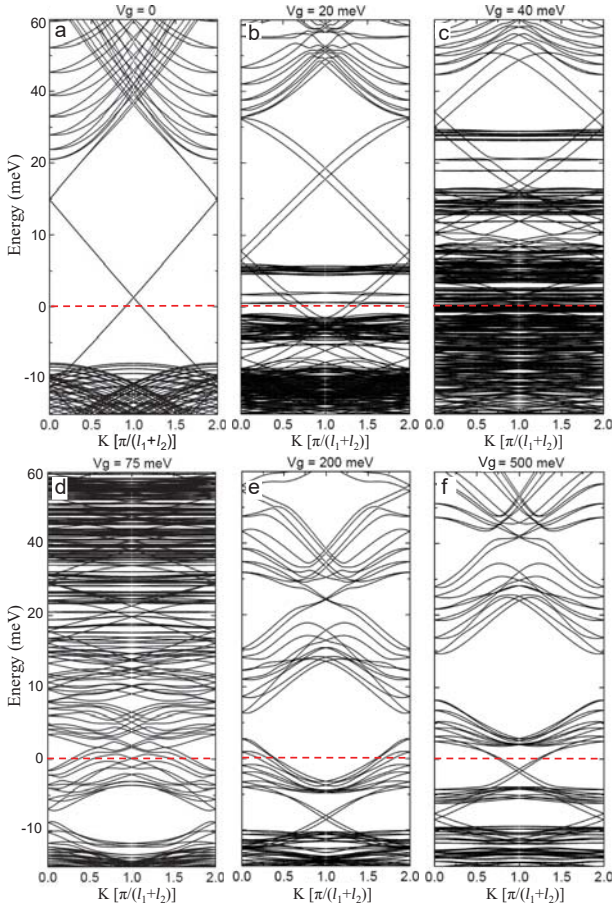

Fig. 4 (a) The band structures of the clean HgTe QW ribbon without any gate voltage or holes. The numerical results are well consistent with those obtained in some previous works.[5,24] The QW ribbon has the same width of Model 3 and the parameter M is set as -10 nm. (b)-(f) The band structures of the HgTe QW ribbon with the increase of the gate voltage V_g from 20 meV to 500 meV. The region of the applied gate voltage has the same configuration shape as the five lines of defected holes and the two zigzag-like boundaries in Model 3 with a reasonable value of M ($\approx$ -10 meV).

perlattices were observed successfully.[34] The experimental breakthrough supports the realization of the coexistence of two different kinds of Dirac states in our model systems. Besides, we propose another alternative route to fabricate HG: applying gate voltage or external electric field on the clean HgTe QWs in a pattern. The gate voltage has the same configuration shape as the defect region with five lines of hexagonal holes and two zigzag-like boundaries in Model 3. To confirm our idea, in Fig. 4, we calculate the band structures of the HgTe QWs covered by the voltage gate, and find that as the gate voltage V_g is increased to 500 meV, the band structure can be compared with that of Model 3 with a suitable value of M ($\approx$ -10 meV). We noted that the top gate voltage as high as 5 V has been successful applied on the HgTe QWs to control carrier density in experiments,[35,36] indicating the feasibility of creating novel QSH state in gate voltage.

In summary, we have constructed HgTe QWs with defect arrays in honeycomb pattern HG and determined their electronic properties through four-band tight-binding calculations. Interesting QSH state can be generated and manipulated such as: (i) HgTe QWs with HG have multiple Dirac cones, regardless of the QW thickness, which provides a feasible way to realize the QSH effect for particular use; (ii) the QSH state produced by HG may exist in regions without HG, allowing to separate the generation and operation of QSH states from far away terminals and (iii), the HgTe QWs with HG can be considered as the first example of the coexistence of the Dirac cones with different physical mechanisms, and offer an useful platform for studies of the QSH effect in nanosystems. Although the four-band model might be too simple to describe atoms at the edges, we noted that states from those atoms most form flab bands and the Dirac states we discussed in this work hence should be reasonably described. We believe our predictions here may inspire experimental tries and should open a new way for the design of topological status of materials.

Conflicts of interest

There are no conflicts to declare.

Acknowledgements

This work is support by as part of the SHINES, an Energy Frontier Research Center founded by the U. S. Department of Energy, Office of Science, Basic Energy Science under Award SC0012670. H.F also acknowledges support from the National Natural Science Foundation of China (Nos. 11274128 and 11774104).

Notes and references

1 M. Z. Hasan and C. L. Kane, *Rev. Mod. Phys.*, 2010, **82**, 3045–3067.
2 L. Fu and C. L. Kane, *Phys. Rev. B*, 2007, **76**, 045302.
3 C. L. Kane and E. J. Mele, *Phys. Rev. Lett.*, 2005, **95**, 226801.
4 X.-L. Qi and S.-C. Zhang, *Rev. Mod. Phys.*, 2009, **95**, 066803.
5 B. A. Bernevig, T. L. Hughes and S. C. Zhang, *Science*, 2006, **314**, 1757–1761.
6 M. König, S. Wiedmann, C. Brüne, A. Roth, H. Buhmann, L. W. Molenkamp, X.-L. Qi and S.-C. Zhang, *Science*, 2007, **318**, 766–770.
7 P. Soltan-Panahi, J. Struck, P. Hauke, A. Bick, W. Plenkers, G. Meineke, C. Becker, P. Windpassinger, M. Lewenstein and K. Sengstock, *Nat. Phys.*, 2011, **7**, 434–440.
8 Z. F. Wang, Z. Liu and F. Liu, *Nat. Commun.*, 2013, **4**, 1471.
9 K. K. Gomes, W. Mar, W. Ko, F. Guinea and H. C. Manoharan, *Nature*, 2012, **483**, 306–310.
10 C.-H. Park and S. G. Louie, *Nano Lett.*, 2009, **9**, 1793–1797.
11 M. Gibertini, A. Singha, V. Pellegrini, M. Polini, G. Vignale, A. Pinczuk, L. N. Pfeiffer and K. W. West, *Phys. Rev. B*, 2009, **79**, 241406.
12 E. Kalesaki, C. Delerue, C. M. Smith, W. Beugeling, G. Allan and D. Vanmaekelbergh, *Phys. Rev. X*, 2014, **4**, 011010.
13 W. Beugeling, E. Kalesaki, C. Delerue, Y.-M. Niquet, D. Vanmaekelbergh and C. M. Smith, *Nat. Commun.*, 2014, **6**, 6316.
14 P.-F. Liu, L. Zhou, T. Frauenheim and L.-M. Wu, *Nanoscale*, 2017, **9**, 1007–1013.
15 C. X. Liu, T. L. Hughes, X.-L. Qi, K. Wang and S.-C. Zhang, *Phys. Rev. Lett.*, 2008, **100**, 236601.
16 I. Knez, R.-R. Du and G. Sullivan, *Phys. Rev. Lett.*, 2012, **109**, 186603.
17 M. P. Boneschanscher, W. H. Evers, J. J. Geuchies, T. Altantzis, B. Goris, F. T. Rabouw, S. A. P. van Rossum, H. S. J. van der Zant, L. D. A. Siebbeles, G. V. Tendeloo, I. Swart, J. Hilhorst, A. V. Petukhovl, S. Bals and D. Vanmaekelbergh, *Science*, 2014, **134**, 1377–1380.
18 W. H. Evers, B. Goris, S. Bals, M. Casavola, J. de Graaf, R. van Roij, M. Dijkstra and D. Vanmaekelbergh, *Nano Lett.*, 2013, **13**, 2317–2323.
19 K. Chang and W.-K. Lou, *Phys. Rev. Lett.*, 2011, **106**, 206802.
20 V. Krueckl and K. Richter, *Phys. Rev. Lett.*, 2011, **107**, 086803.
21 J. Wang, B. Lian, H. Zhang, Y. Xu and S.-C. Zhang, *Phys. Rev. Lett.*, 2013, **111**, 136801.
22 M. König, H. Buhmann, L. W. Molenkamp, T. Hughes, C.-X. Liu, X.-L. Qi and S.-C. Zhang, *J. Phys. Soc. Jpn.*, 2008, **77**, 031007.
23 C. Wu and S. D. Sarma, *Phys. Rev. B*, 2008, **77**, 235107.
24 H. Jiang, L. Wang, Q.-F. Sun and X. C. Xie, *Phys. Rev. B*, 2009, **80**, 165316.
25 E. G. Novik, A. Pfeuffer-Jeschke, T. Jungwirth, V. Latussek, C. R. Becker, G. Landwehr, H. Buhmann and L. W. Molenkamp, *Phys. Rev. B*, 2005, **72**, 035321.
26 L.-H. Hu, D.-H. Xu, F.-C. Zhang and Y. Zhou, *Phys. Rev. B*, 2016, **94**, 085306.

27 A. H. C. Neto, N. M. R. Peres, K. S. Novoselov and A. K. Geim, *Rev. Mod. Phys.*, 2009, **81**, 109–162.
28 C. Wu, D. Bergman, L. Balents and S. D. Sarma, *Phys. Rev. Lett.*, 2007, **99**, 070401.
29 H.-H. Fu, J.-T. Lü and J.-H. Gao, *Phys. Rev. B*, 2014, **89**, 205431.
30 H.-H. Fu, J.-H. Gao and K.-L. Yao, *Nanotechnology*, 2014, **25**, 225201.
31 B. Zhou, H.-Z. Lu, R.-L. Chu, S.-Q. Shen and Q. Niu, *Phys. Rev. Lett.*, 2008, **101**, 246807.
32 L. Brey and H. A. Fertig, *Phys. Rev. B*, 2006, **73**, 235411.
33 S. Wang, D. Scarabelli, Y. Y. Kuznetsova, S. J. Wind, A. Pinczuk, V. Pellegrini, M. J. Manfra, G. C. Gardner, L. N. Pfeiffer and K. W. West, *Appl. Rev. Lett.*, 2016, **109**, 113101.
34 S. Wang, D. Scarabelli, L. Du, Y. Y. Kuznetsova, L. N. Pfeiffer, K. W. West, G. C. Gardner, M. J. Manfra, V. Pellegrini, S. J. Wind and A. Pinczuk, *Nat. Nanotech.*, 2018, **13**, 29–33.
35 X. C. Zhang, A. Pfeuffer-Jeschke, K. Ortner, V. Hock, H. Buhmann, C. R. Becker and G. Landwehr, *Phys. Rev. B*, 2001, **63**, 245305.
36 J. Hinz, H. Buhmann, M. Schfer, V. Hock, C. R. Becker and L. W. Molenkamp, *Semicond. Sci. Technol.*, 2006, **21**, 501.